Dirk E. Boonzajer Flaes, Jan Stopka,
Sergey Turtaev, Johannes F. de Boer, Tomáš Tyc, Tomáš Čižmár

S1.   PROPAGATION INVARIANT MODES IN A BENT FIBER

To describe the effect of fiber bending on light modes propagating through a fiber quantitatively, we will initially consider scalar waves and account for polarization later. A scalar wave Ψ is governed by the Helmholtz equation $(\Delta + k^2 n^2)\Psi = 0$, where n is the refractive index. The wave can be separated as $\Psi = \psi(x,y) \exp(i\beta z)$, where z is the coordinate along the fiber axis, β is the propagation constant, and ψ is governed by the transverse equation

$$[\Delta_\perp + k^2 n^2 - \beta^2]\psi = 0 \,. \qquad (9)$$

Here $\Delta_\perp = \partial_x^2 + \partial_y^2$ denotes the transverse part of the Laplacian. For the parabolic refractive index profile (1), Eq. (9) separates both in Cartesian and polar coordinates. The PIMs separated in polar coordinates are given by Eq. (2) with propagation constants (3).

Now consider scalar waves in a uniformly bent fiber in the xz plane with curvature ρ, with the center of curvature at the point $(1/\rho, 0, 0)$. The local propagation constant is then no longer uniform across the fiber cross-section, but depends on x as $k_z(x) = \beta'/(1 - \rho x)$, where β' is the propagation constant on the axis of the bent fiber [1]. Replacing β by $k_z(x)$ in Eq. (9) and using Eq. (1), we get the following equation for the bent fiber scalar PIMs:

$$\left[\Delta_\perp + k^2 n_0^2 \left(1 - \frac{x^2 + y^2}{b^2}\right) - \frac{\beta'^2}{(1 - \rho x)^2}\right]\psi = 0 \,. \quad (10)$$

If we make a substitution $x = x' - \Delta x$, where $\Delta x \equiv \beta'^2 \rho/(\alpha^2 + 3\beta'^2 \rho^2)$ and α is defined under Eq. (2), we get, after neglecting terms of the order ρ^4 and higher, the equation

$$\left[\Delta_\perp + k^2 n_0^2 - \alpha^2(x'^2 + y^2) - 3\beta'^2 \rho^2 x'^2 \right.$$
$$\left. + \frac{\beta'^4 \rho^2}{\alpha^2} - \beta'^2\right]\psi = 0 \,. \quad (11)$$

Eq. (11) corresponds in its form to Eq. (9) with x replaced by x', with β^2 replaced by $\beta'^2 - \beta'^4 \rho^2/\alpha^2$, and with an additional term $3\beta'^2 \rho^2 x'^2 \psi$. This shows that the effect of fiber bending is threefold. First, the center of the effective index profile is shifted in the negative x-direction (i.e., towards the outer side of the bend) by the distance Δx defined above; the modes in the bent fiber will, accordingly, also be shifted by Δx towards the outer side of the bend. Second, the steepness of the parabolic index profile in the x-direction gets slightly increased due to the additional term $3\beta'^2 \rho^2 x'^2$ in Eq. (11); for small curvatures ρ this term can be regarded as a perturbation. Third, there appears a term $\beta'^4 \rho^2/\alpha^2$ that will lead to an additional shift of the propagation constants.

Next we have to account for the influence of light polarization. As it is well known, the polarization influences propagation constants, which is an effect known as spin-orbital (SO) interaction. For a straight fiber, the corresponding equation for electromagnetic waves still separates in cylindrical coordinates but no more in Cartesian ones. For the parabolic index profile (1) in the weakly-guided regime, the propagation constants (3) are shifted due to SO interaction by the amount [2]

$$\Delta\beta_{l,m,\sigma} = -\frac{l\sigma + 1}{2 k n_0 b^2} \,, \qquad (12)$$

where $\sigma = \pm 1$ for the right- and left-handed circular polarization state, respectively.

Now if the fiber is bent, both effects of the SO interaction and the effective change of the refractive index described above are present simultaneously. For small curvatures, the SO interaction is dominant and the effect of fiber bending can be regarded as a small correction; then we can use perturbation theory of the first order to evaluate the effect of the additional term $3\beta'^2 \rho^2 x'^2$ in Eq. (11). For that, we need to evaluate the mean value of x'^2 for the LG PIMs. This can be done if we employ the equivalence of Eq. (9) with the stationary Schrödinger equation for a 2D harmonic oscillator with frequency α (when $\hbar$ and particle's mass are set to unity). Then the operator $\Delta_\perp - \alpha^2(x'^2 + y^2)$ in Eq. (11), up to the factor $-1/2$, is equal to the Hamiltonian $-\Delta_\perp/2 + \alpha^2(x'^2 + y^2)/2$ of a 2D harmonic oscillator with equilibrium position $(x, y) = (-\Delta x, 0)$. Now, by the virial theorem, the mean potential energy $\langle \alpha^2(x'^2 + y^2)/2 \rangle$ comprises half of the oscillator total energy, i.e., of $\alpha(|l|+2m+1)$ in case of the LG state $|l, m\rangle$. Moreover, the probability distribution in the LG states is isotropic, so the energy is distributed equally between the x and y degrees of freedom. From these facts we find that $\langle x'^2 \rangle = (|l| + 2m + 1)/(2\alpha)$. Going back to Eq. (11) and substituting the relevant terms, we get

$$k^2 n_0^2 - 2\alpha Q - \frac{3\beta'^2 \rho^2 Q}{2\alpha} + \frac{\beta'^4 \rho^2}{\alpha^2} - \beta'^2 = 0 \,, \qquad (13)$$

where we have denoted $Q = |l| + 2m + 1$ for convenience. When we solve this equation for β', neglect terms of the fourth order in ρ and take advantage of Eq. (3), we get finally for the propagation constants of the PIMs in the bent fiber

$$\beta' = \beta + \rho^2 \left(\frac{k n_0 b^2}{2} - \frac{9b(|l| + 2m + 1)}{4}\right) \,, \qquad (14)$$

where β is the propagation constant (3) of the PIM in the straight fiber with the same numbers l, m. Using Eq. (12) and expanding the square root, we can write the

Common optical components

Item	Part number
L1, L7, L8	A240TM-C
L2	AC254-400-C-ML
L3	AC254-300-C-ML
L5	AC254-150-C-ML
SMF	P1-980A-FC-1
QWP1, QWP2	WPC10M-1064
HWP	WPC10M-1064
NPBS1, NPBS2	CM1-BS014
M1-3	BB1-E03

Altered optical components

Item	Fiber	Rod
MMF/GL	GIF50C	LRL-035-P375
MO1	Plan N 20x	UPLSAPO 10x
MO2	Plan N 20x	Plan N 10x
L4	AC254-200-C-ML	AC254-150-C-ML
L6	AC254-150-C-ML	AC254-150-A-ML

TABLE S1. List of optics involved in the experiment. Common components have been listed in the top half, optics that were changed to measure either fiber or rod have been listed in the lower half. All part numbers except for the microscope objectives are Thorlabs part numbers. All microscope objectives were manufactured by Olympus.

Spot-scanning fibers

Fiber	Part number	# modes
SI fiber	FG050UGA	500
GI fiber 1	GIF50C	300
GI fiber 2	GIF625	700

TABLE S2. Fibers employed for the spotscanning experiment as described in Fig. 4. All part numbers are Thorlabs part numbers.

total propagation constant for the vector PIM (l, m, σ) as

$$
\beta'_{l,m,\sigma} = kn_0 \left(1 + \frac{\rho^2 b^2}{2}\right)
$$
$$
- \left(\frac{1}{b} + \frac{9\rho^2 b}{4}\right)(|l| + 2m + 1) - \frac{l\sigma + 1}{2kn_0 b^2}. \quad (15)
$$

We can also compare the order of correction to propagation constants due to bending and due to SO interaction. A simple analysis shows that the two corrections, namely $9\rho^2 bQ/4$ and $(l\sigma + 1)/(2kn_0 b^2)$, become comparable for curvatures of $\rho = 1/\sqrt{2kn_0 b^3}$, which is about $(1\ \text{cm})^{-1}$ for a typical fiber. The above analysis is valid for curvatures smaller than this.

S2. EXPERIMENTAL DETAILS

S2-I. Waveguide characteristics

The PI-rod has been manufactured using a process where initially a glass rod is taken with a constant refractive index profile, which is then doped using a salt bath, resulting in a very smooth parabolic refractive index profile. The rod has a diameter of 350 µm (Selfoc LRL–035–P375–0–0–0–0), with a NA of 0.12. The manufacturer of the PI rod specifies that the quality of the refractive index profile goes down in the outer 20-30% of the rod.

The graded index fiber is a standard communication graded-index fiber, with an NA of 0.275, which is manufactured using an MCVD process, for which it is difficult to prevent a characteristic dip in the core of the refractive index profile.

Even though the rod (5.6 cm) is longer than the fiber (20 mm), the refractive index profile of the fiber is much steeper. To properly compare waveguide lengths we compare the modal phase difference between subsequent waveguides modes, which scales with L/b. When a pattern is projected on the proximal end of a graded-index medium, it is imaged again inside the rod after a length $2\pi b$, called the pitch length. The pitch length of the graded index rod is about 1.4 cm, whereas the pitch length of the fiber is about 1 mm. Therefore the rod is about 3.7 pitches long while the fiber is roughly 20 pitches long. For an ideal comparison, the waveguides would have been cut to the same pitch length. However, cutting a fiber of only a millimeter would have not been possible, and a rod with a length of roughly 28 cm would also be very difficult to handle or manufacture.

S2-II. Experimental setup

The optical setup for the fiber analysis is analogous to the setup used in Ref. [1]. Since our study only exploits one circular polarization (which has been shown to remain conserved while light propagates through a fiber) our system only uses a single circular polarization pathway, which is shown in Fig. S5. There is a 45° rotation angle between the camera and the SLM, which is taken into account in the analysis. The SLM is located in the farfield of the frontal fiber facet. To measure the transmission matrix, a hologram is displayed on the SLM creating two points in the farfield, one of which is imaged onto the frontal fiber facet, called the scanning beam, while the other one is coupled into a single mode fiber and used as a reference. The scanning beam is sequentially repositioned across the facet of proximal end, and the resulting output field distribution is obtained by interfering the output field with a reference beam on the camera. More details on this procedure can be found in [1, 3]. As the number of scanning points is limited due to the relatively slow update rate of the SLM, the spacing of the focal points on the proximal end and the pixel size on the distal end have to be optimized for the medium under investigation, as explained below.

S2-III. Modal cutoff conditions

To properly design the optical system required to characterize the waveguides, it is important to know the sampling requirements on the setup. This is determined by the number of modes that travel through the waveguide. While for a step-index fiber a clear cutoff of supported modes [2] can be defined, this is not obvious for a parabolic refractive index profile, extending to infinity. However, our waveguides have a finite spatial extent and as such the number of modes will be limited to modes that mainly travel within the core of the waveguide. PIMs that are very near the edge of the air–glass or core/cladding interface will likely be severely distorted.
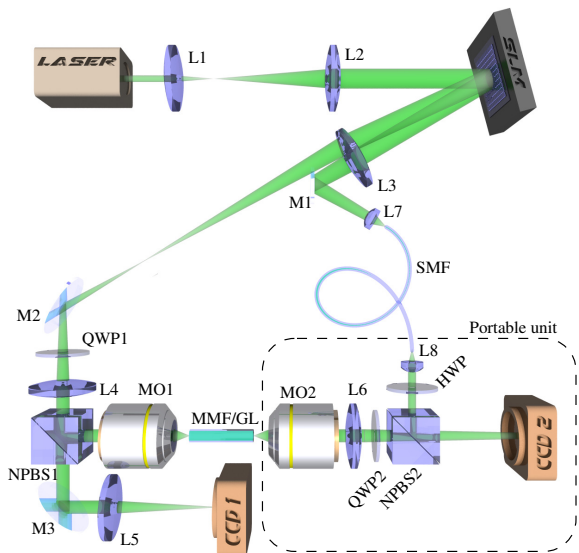
FIG. S5. Optical setup employed to measure transmission matrices. Electronic components: CCD 1 and 2: Basler piA640-210gm. SLM: Boulder Nonlinear Systems / Meadowlark Optics HSDPM512 DVI. Optical components are dependent on the MMF under investigation, and are listed in Table S1. When measuring the fiber, optics were present between L3 and L4 to control polarization of the input state, as in Ref.[1], which were not used and which are not shown. They did not support scanning a larger field of view, and have been removed for the rod measurements. To employ the system with a bent fiber, the imaging setup on the distal end is designed as a portable unit and can be moved on the table.

Therefore we confined the analysis to the central part of the rod only. To limit our analysis to modes that are properly guided, we demand that 99% of the amplitude of the mode falls within 75% of the core diameter in the case of the rod (the area with a high quality refractive index profile as specified by the manufacturer), and within the full core diameter in case of the fiber. In case of the graded index rod this means that the highest radial mode number we expect to be undistorted by boundary effects to be at $m_{\max} = 15$ for $l = 0$, and $|l_{\max}| = 44$ for $m = 0$, as shown in Fig. S6.

S2-IV. Optical design considerations

Ideally, the transmission matrix should be measured with a large enough spatial extent and a sufficiently fine spacing that all the modes of interest up to and including $m_{\max}$ and $l_{\max}$ can be sampled and analyzed. However, with our current setup, this would result in a transmission matrix size that is not feasible due to technical limitations, mainly with respect to the acquisition time. The number of scanned points on the proximal end was limited to 85×85 points. Therefore, it is important to optimize the sampling area and pixel spacing of the transmission matrix measurement in such a way that the optimal amount of information can be extracted from the minimal number of measurements.

If a PIM is not properly sampled, the fiber is not presented with a perfect eigenmode. Similar to presenting the fiber with a misaligned mode, this will lead to apparent mode coupling, as discussed in the main article. In order to excite a given mode with sufficient resolution on the proximal end, and in order to detect a mode unambiguously on the distal end, similar selection criteria were employed as for determining the highest supported PIMs in the preceding section: The physical extent of the PIM needs to be sampled (real space condition), and this area has to be scanned with a sufficiently fine spacing that all features within the PIM are sufficiently expressed (Fourier space condition). To check the real space condition, a larger field of view was sampled, verifying that no more than 1% of the total amplitude of the PIM was present outside of the sampled area. To check the Fourier space condition, every mode was sampled at a half the pixel spacing, and the 2D fast Fourier transform (FFT) was computed. In this case, a mode was discarded if more than 1% of the total amplitude of the PIM was outside the area dictated by half the Nyquist frequency. The exact cutoff conditions are therefore dependent on the magnification of the imaging systems, and on the alignment parameters.

In order to optimize the design of the optical setup, for every available combination of lenses the number of modes that could be sampled and analyzed was computed, and the combination of optics that led to the highest number of excitable modes was used.

For the available combinations of optics, the optimal pixel pitch on the proximal end was 4.6 μm. On the distal end, the sampling was fixed at 6.2 μm, due to the curvature of the reference beam. The highest supported radial and angular PIM after optimizing alignment are shown in Fig. S7. In both cases the PIM approaches the edge of the scanned area by the SLM, as well as containing features which are too fine to be sampled properly on the camera.

Even though it was impossible to excite all supported PIMs, the final modal cutoff conditions for perfect alignment ran between $|l| = 42$ for $m = 0$, and $m = 13$ for $|l| = 0$. This represents a significant fraction of all the PIMs of interest.

S3. OPTIMIZATION ALGORITHMS

S3-I. Misalignment parameters

After measuring the transmission matrix in a point basis, the correct alignment parameters still have to be found in order to understand the transmission matrix in terms of PIMs. The optimization strategy is very similar to the one used in Ref. [1], but not identical. A brief overview of the procedure is given here and the differences are highlighted.

First, after measuring the transmission matrix TM in a point basis, the same method as described in the methods section of Ref. [1] was used for the initial alignment, resulting into a matrix of 3969 (63×63) input points by 4096 (64×64) output points for circular polarized light. Unlike the previous system, only a single polarization was taken into account. Therefore, spin-orbit interaction cannot be distinguished from a rotation between SLM and camera and it was not analyzed in the procedure.
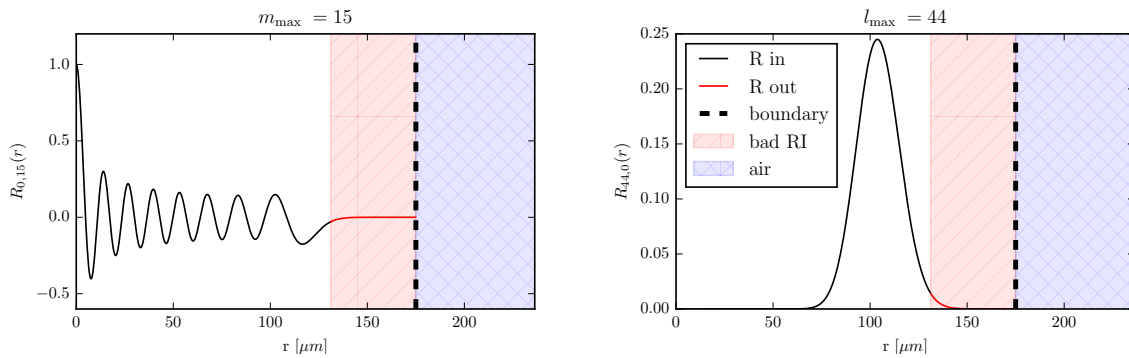
FIG. S6. Radial part $R_{l,m}(r)$ of the highest supported radial (left) and angular (right) PIM for the graded-index rod. Blue shading indicates the area outside of the rod, red shading indicates the area with a low-quality refractive index profile. The black line indicates the amplitude of the radial part, red indicates the amplitude outside in the area with a low-quality refractive index.
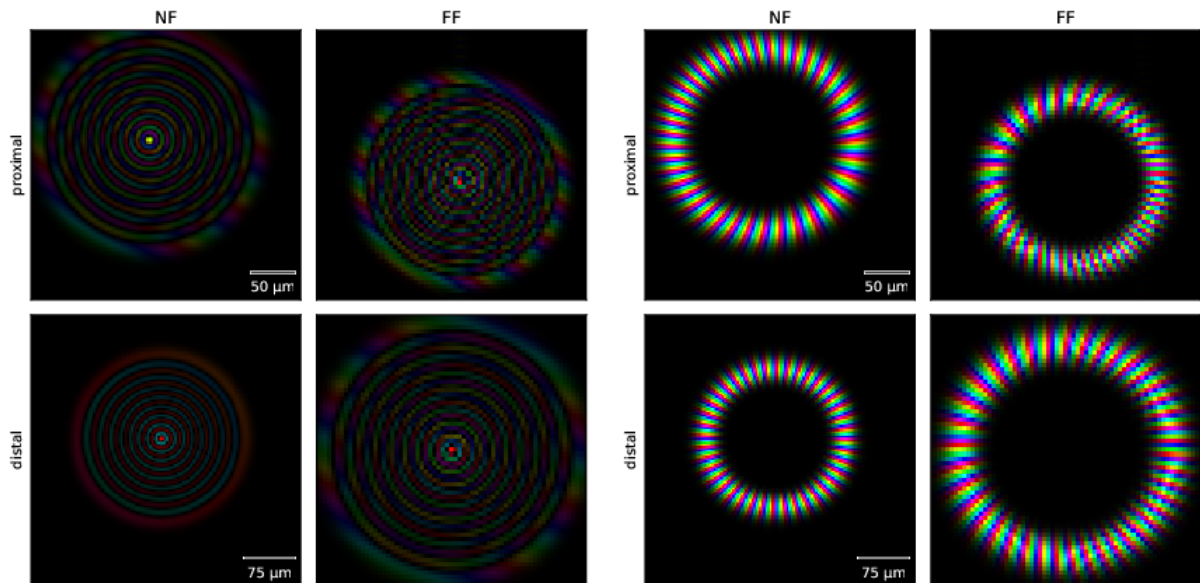

FIG. S7. Sampling of highest order radial (left) and angular (right) PIM included in the analysis after optimal alignment of the rod. Both groups of four represent the different constraints, and the black square indicates the area that has been sampled while measuring the transmission matrix. For both groups of four: Top left: PIM sampled on the proximal end of the fiber (real space constraint on proximal end), Bottom left: same PIM sampled on the distal end of the fiber (real space constraint on distal end). Top right: Farfield of the PIM sampled on the proximal end (Fourier space constraint on proximal end). Bottom right: Farfield of the PIM sampled on the distal end (Fourier space constraint on distal end). For a PIM to be properly guided, it needs to fit within all of these images. In this case, the Fourier space constraint on the distal end is just met for the PIMs under investigation. Also, the PIMs hit the edge of our sampled domain on the proximal end.

Initially, after converting the TM into a mode basis, the power on the diagonal (modal performance) is still only around 1%, due to residual misalignment. Therefore, a separate alignment procedure is employed to find the optimal location and size of the PIMs. In total, this optimization procedure needs to find eleven parameters: waveguide location (3D) on proximal and distal end, and angle of incidence (2D) on proximal and distal end, and the overall steepness of the refractive index profile (1D). Instead of attempting to optimize all of these parameters at the same time, only the parameters corresponding to a particular domain, (for instance proximal position or distal angle) are optimized at the same time for reasons of computational efficiency. The procedure is iteratively repeated until it converges using a Nelder-Mead simplex algorithm. As this is a minimization algorithm, instead

of the relative power on the diagonal P, $-P$ was used as a cost function. Previously P^{-1} was used. This was not seen to have any significant influence on the result. Also, previous work employed explicit minimization of PIMs close to the diagonal, which was not implemented in our analysis.

One of the challenges of the optimization routine is that it takes very long to converge, especially if a lot of modes are involved. The previous routine attempted to optimize misalignment parameters using all supported PIMs at the same time, but we found that a reasonably accurate guess can be obtained by first selecting only a few low-order modes and doing a few rapid iterations based on those. Then the number of modes can be increased for a more accurate estimate. After every iteration, the $l_{\max}$ was increased by two and $m_{\max}$ by one
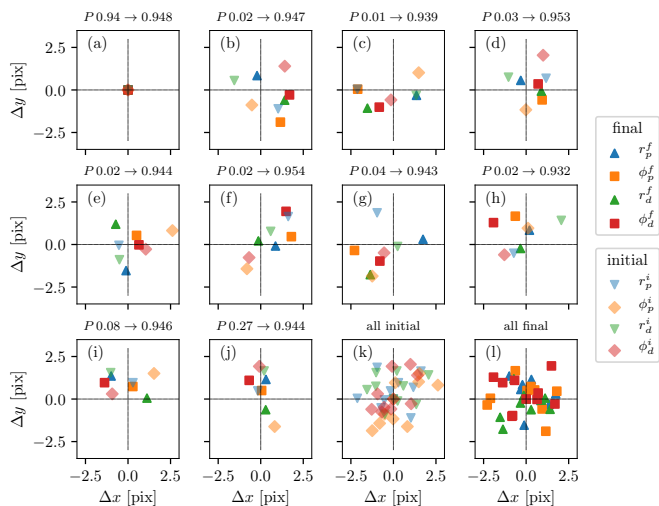
FIG. S8. Indication of stability of the solution to perturbing input misalignments, relative to the optimized position used in the paper. (a): Optimized alignment used in the further analysis. (b-j): Final alignment parameters after perturbing the final state in (a) by a total of 10 pixels, as discussed in the text. The initial and final performance P is printed on top of the figure. (k): All perturbed initial alignment parameters. (l): All final alignment parameters. Labels: r_p, r_d represent spatial alignment parameters on proximal and distal end, ϕ_p, ϕ_d are the angular misalignments. Even though the the final P is on a similar level, different initial misalignment parameters lead to different final misalignment parameters.
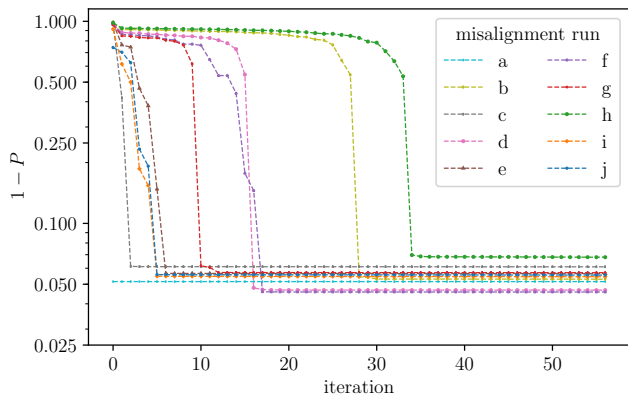

FIG. S9. Optimization trace for input misalignments (a-j) in Fig. S8. The performance is plotted after optimizing every invidividual misalignment parameter. Even though there is a small variation in the number of steps required to find the misalignment, the final modal performances P are very similar.

until the sampling limit was reached. Optimizing the refractive index profile steepness was only started after 20 iterations of the optimization routine. Previously, the fiber parameters needed a different optimization metric in order not to lead to solutions featuring a small number of PIMs. This is not required for the analysis of the graded index waveguide.

As the modal cutoff conditions of the waveguide are determined by the pixel spacing it is important to be cautious about sampling artefacts, which could lead to apparent mode coupling. In previous work, all the modes
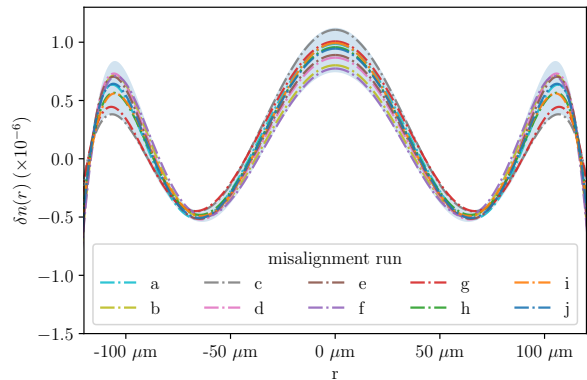

FIG. S10. Optimized refractive index profile differences for different optimization runs as described in Fig. S8. The shaded region indicates the 95% confidence interval. The final parameters have a small influence on the resulting refractive index profile.

were computed for a single location and shifting the center and tilt of all the modes was achieved using an interpolation matrix $\mathbf{C}$. This might lead to interpolation artefacts, however. Therefore we chose to sample the modes after every step of the iteration using Eq. (2).

Due to technical constraints with respect to the experimental setup, complete characterization of the rod was not possible, as the number of modes that can propagate in the rod exceed the number of modes that we can analyze using our sampled transmission matrix. Therefore, some inaccuracy of the final misalignment parameters is to be expected, and multiple combinations of misalignment parameters can lead to similar performance.

In order to give an idea of the accuracy of the reconstructed alignment parameters, we perturbed the final alignment parameters of the optimization routine in 2D, and ran the optimization routine again using the perturbed misalignment parameters as the initial locations. To keep the optimization time within a couple of hours, the sum of the disturbances was kept at 10 pixels. This is a large enough disturbance that P is initially only a few percent, but it is not so much disturbed that the optimization strategy takes more than an hour. If the system was fully determined, different initial conditions would lead to the same final conditions. However, as we show in Fig. S8 and S9, the final misalignment parameters differ for varying input misalignments.

The grin rod is acting like very good lens and as such, depending on the length or the rod, some of the misalignment parameters are coupled. For instance, if the waveguide were replaced with an imaging system imaging the frontal facet onto the distal facet, it would always be possible to shift the input modes by the same amount as the output modes, provided that the analyzed modes do not hit the edges of the lens. Therefore, when the lens is larger than the analyzed area there are multiple combinations of misalignment parameters that lead to very similar performance. Future research could exploit this ambiguity in order to come up with a faster optimization scheme. The final P is very similar (Fig. S9) and for our analysis this ambiguity is mainly an indication that the rod is of a very high optical quality.
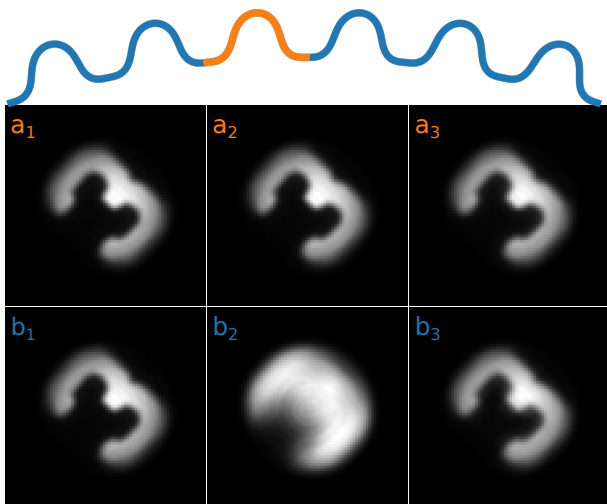
FIG. S11. Simulation of the scanning imaging experiment in Fig.4, tight bend, for the fiber indicated as GRIN~300 modes. Top: Indication of simulated fiber layout for the short fiber (the single orange sigment) and the long fiber (blue, six copies of the short segment). a_1: simulated imaging performance for a straight fiber, a_2: bent fiber using the straight fiber TM, a_3: imaging using the length correction described by Eq. (7). $b_{1,2,3}$: Same simulation for the long fiber. For the long fiber, the bending compensation clearly results in the restoration of the image quality.

S3-II. Changes to the refractive index profile optimization routine

The procedure used to fit the refractive index profile abberations, as shown in Fig. 2, was nearly identical to the one used in [1]. For abberating functions, a basis of Zernike modes $Z_n(r/r_0)$ was employed, where r_0 is a scaling factor, fixed at 125 µm, the effective radius that was analyzed. We repeated the analysis for all the final locations indicated in Fig. S8. This only resulted in very small deviations in the resulting refractive index modulations, indicated in Fig. S10. The confidence interval was taken as two times the standard deviation in the individually optimized refractive index profiles.

S4. SPOT-SCANNING EXPERIMENT

The experimental procedure for the spot-scanning experiment was identical to the one outlined in Ref. [1, Supplementary movie 7]. It consists of the following steps:

1. Using the setup in Fig. S5, acquire a transmission matrix T for the fiber, allowing for some room in between the distal end of the MMF and MO2 for later sample insertion.

2. Insert the sample (the transmissive part of a reflective USAF target) between MMF and MO2.

3. Using the SLM, display the required input fields (columns of $T^\dagger$) sequentially in order to scan a spot on the distal end of the fiber.

4. At every spot position, record the total transmitted intensity on CCD2 (sum of all camera pixel values).

5. Arrange the measured intensities by focal location, forming an image (Fig. 4).

As described in Ref. [1, Supplemental material], it would also be possible to employ the only open port of NPBS1 to do "true" endoscopic imaging, but it requires careful calibration of the internal reflections in the setup, and it is not essential to demonstrate the bending sensitivity. To bend the fiber, the portable unit in the setup can be moved towards MO1, and only the imaging experiment was repeated. The fiber parameters are shown in Table S2.

To compare the theoretical imaging performance with the experimental results for the strongest bend in Fig. 4, a mathematical simulation of imaging through a bent fiber is performed, by numerically reproducing the process of the scanning imaging experiment. The brightness of the i-th pixel of resulting image can be computed as

$$I_i = \left| PS^\dagger T'T^{-1} Sv_i \right|^2. \tag{16}$$

Here P is a binary mask representing the target, T is the calculated TM of the straight fiber in the PIM basis, T' is the calculated TM of the same fiber bent according to the experiment calculated in the basis of PIMs of the straight fiber, S is a matrix representing the transformation from the basis of focused spots into the basis of PIMs (the converse transformation is represented by $S^\dagger$) and v_i is a vector in the basis of focused spots representing the spot at the position of i-th pixel.

The TM of the bent fiber T' is calculated as a product of 300 TMs of short segments of fiber with constant curvature. T can be modified to account for the effective length increase as described by Eq. (7). However, the effective length increase is only 17 µm, and as such the effect is minimal. Results of the simulation are shown in Fig. S11a. We attribute the decreased imaging performance observed in the experiment to imperfections in the refractive index profile. To demonstrate the expected performance of the bending correction for an ideal parabolic-index MMF, we simulate the imaging procedure for a longer fiber consisting of six identical copies of the short geometry, shown in Fig. S11b, using 1800 segments. In this case it is clear that the applied correction for the effective length increase leads to almost complete restoration of the original image quality.

[1] M. Plöschner, T. Tyc, and T. Čižmár, Nature Photonics 9 (2015), 10.1038/nphoton.2015.112.

[2] A. W. Snyder and J. Love, *Optical Waveguide Theory*, 1st ed. (Springer, 1983).

[3] T. Čižmár and K. Dholakia, Opt. Express 19, 18871 (2011).